ARTICLE

Mapped Finite Element Discrete Variable Representation†

De-quan Yu[a,b], Shu-lin Cong[a*], Dong H. Zhang[b], Zhi-gang Sun[b*]

a. School of Physics and Optoelectronic Technology, Dalian University of Technology, Dalian 116024, China

b. State Key Laboratory of Molecular Reaction Dynamics and Center for Theoretical and Computational Chemistry, Dalian Institute of Chemical Physics, Chinese Academy of Science, Dalian 116023, China

(Dated: Received on October 23, 2013; Accepted on December 13, 2013)

Efficient numerical solver for the Schrödinger equation is very important in physics and chemistry. The finite element discrete variable representation (FE-DVR) was first proposed by Rescigno and Mc-Curdy [Phys. Rev. A **62**, 032706 (2000)] for solving quantum-mechanical scattering problems. In this work, an FE-DVR method in a mapped coordinate was proposed to improve the efficiency of the original FE-DVR method. For numerical demonstration, the proposed approach is applied for solving the electronic eigenfunctions and eigenvalues of the hydrogen atom and vibrational states of the electronic state $^3\Sigma_g^+$ of the Cs_2 molecule which has long-range interaction potential. The numerical results indicate that the numerical efficiency of the original FE-DVR has been improved much using our proposed mapped coordinate scheme.

Key words: Discrete variable representation, Mapped Fourier method, Ultra-cold atomic photoassociation, Schrodinger equation solver, Singularity of Coulomb potential

I. INTRODUCTION

Efficient numerical methods for solving the Schrödinger equation are important for describing a wide variety of physical phenomena, such as photodissociation [1, 2], photoabsorption spectra [3−7], pre-dissociation [8], resonance Raman spectra [9, 10], reactive scattering [11−13], and molecule-surface scattering [14−17]. A variety of numerical methods have been proposed for solving the Schrödinger equation. One of the key steps for solving the Schrödinger equation is to represent the wave function accurately on finite grid points. Development of the pseudospectral (PS) methods [18, 19] has yielded many efficient schemes to accomplish this goal. These PS schemes include the discrete variable representation (DVR) method [20, 21] and the mapped Fourier grid (MFG) method [22]. Compared to the DVR method, the MFG method automatically enhances the sampling of the grid points in the regions where wavefunction exhibits fast variations, thus it usually provides more reasonable distribution of the grid points. In this perspective, the MFG method is more suitable for long-range potential which requires grid distribution in a non-uniform way. The potential optimized DVR (PODVR) method [23], in principle, can produce grid points in a similar way to the MFG method. However, PODVR method requires the diagonalization of the hamilationian matrix in advance. Sometimes it may be not so convenient.

The MFG method was first proposed for the calculation of eigen-energies of the hydrogen atom by Fattal and co-workers [22]. Later, it was extended to photoassociation spectrum calculation with molecules with long-range potential [24]. Because of its efficiency and accuracy, it has been widely used in a variety of quantum molecular problems [25−27]. Also, much effort has been devoted to the development of this method [28, 29]. Nevertheless, the MFG method still faces some challenges.

The finite element discrete variable representation (FE-DVR) method was first proposed by Rescigno and McCurdy [30] for solving quantum-mechanical scattering problems, based upon the Lobatto-DVR method proposed by Manolopoulos and Wyatt [31]. It has popular applications in time-dependent quantum calculations in the field of atomic and molecular physics [32−44], since the Lobatto DVR method can accurately treat the Coulomb singularity of atoms in spherical coordinate and diatomic molecules in ellipsoidal coordinates [37, 45].

In recent years, there has been a rapid progress in experiments with cold atom samples [46−52]. Many numerical methods have been proposed for treating atomic collisions at very low energy which involves long-range interaction.

In this work, to extend the FE-DVR method for efficiently treating long-range interaction problems, a mapped FE-DVR (M-FE-DVR) method, which uses a

†Part of the special issue for "the Chinese Chemical Society's 13th National Chemical Dynamics Symposium".

*Authors to whom correspondence should be addressed. E-mail: shlcong@dlut.edu.cn, zsun@dicp.ac.cn

mapping coordinate procedure to optimize the grids distribution, was put forward. The performance of the M-FE-DVR method is analyzed with solving the electronic eigenfunction and eigenvalue of the hydrogen atom and one dimensional vibrational eigenfunction and eigenvalue of Cs_2 ($^3\Sigma_g^+$) molecule with long-range interaction potential.

In this work, a brief review of the the FE-DVR method and the idea of the M-FE-DVR method were given. Its application on solving eigenstates of the Coulomb problem and the long-range potential of the Cs_2 molecule is shown respectively. The accuracy and efficiency of our proposed M-FE-DVR method are discussed in detail. Atomic units are used throughout unless otherwise stated.

II. MAPPED FINITE ELEMENT DISCRETE VARIABLE REPRESENTATION

A. Mapping procedure

As the MFG method has been extensively described elsewhere [22], here we only present a brief introduction. Let us consider a 1D radical Schrödinger equation for the relative motion of two particles with reduced mass μ on a potential energy curve (PEC) $V(r)$ as the example.

$$\begin{aligned}[\hat{T}+\hat{V}]\psi(r) &= \left[-\frac{1}{2\mu}\frac{\mathrm{d}^2}{\mathrm{d}r^2}+V(r)\right]\psi(r)\\ &= E\psi(r)\end{aligned} \tag{1}$$

The key step of the MFG method is an efficient mapping procedure, which connects the physical, non-equidistant grid r_i with an auxiliary working grid x_i=$f(r_i)$. Under this transformation, the Schrödinger equation can be written in a symmetric form as [24]:

$$\begin{aligned}-\frac{1}{4\mu}\left[\frac{1}{J^2(x)}\frac{\mathrm{d}^2}{\mathrm{d}x^2}+\frac{\mathrm{d}^2}{\mathrm{d}x^2}\frac{1}{J^2(x)}-\frac{7}{2}\frac{J'^2(x)}{J^4(x)}+\right.\\ \left.\frac{J''(x)}{J^3(x)}\right]\phi(x)+V(x)\phi(x)=E\phi(x)\end{aligned} \tag{2}$$

here, $J(x)$ is the Jacobian of the transformation $r\rightarrow x$

$$J(x)=\frac{\mathrm{d}r}{\mathrm{d}x} \tag{3}$$

The aim of applying the mapping procedure is to enhance the sampling efficiency in the regions where the eigenfunctions vary rapidly, thus the eigenfunctions can be represented accurately with fewer grid points totally. One possibility is to estimate the sampling function by a semiclassical, Wentzel-Kramers- Brillouin(WKB)-like argument [24]. In this scheme, the adaptive coordinate x is obtained by integration

$$x(r)=\int_{r_0}^{r}\frac{\sqrt{2\mu[V_{\max}-V(r)]}}{\pi}\mathrm{d}r \tag{4}$$

This scheme has offered accurate numerical results in a variety of applications [53−57], however its accuracy is limited by some undesirable side-effects of the WKB approximation in the region close to the classical turning points. Especially, when the potential $V(r)$ is not analytical and varies dramatically steeply, the $x(r)$, $J(x)$ and its derivatives will be difficult to be evaluated accurately. Another approach to find the optimal adaptive grid is to make an educated guess.

Since the resulting physical grid density is proportional to the gradient of $x(r)$, $x(r)$ should be steep in the strong interaction region but in the asymptotic region $x(r)$ should be flat. Application of $x(r)$ following an educated guess as the mapped function can avoid the undesirable side-effects of the WKB approximation. As the mapping function $x(r)$ has an analytical form, $x(r)$ and $J(x)$ and its derivatives are easy to accurately evaluate. In this work, we adopt the mapping function suggested in Ref.[58].

$$x(r)=(r-\alpha)^{1/p} \tag{5}$$

where α is a constant to tune the grid points distribution. In this work, p is set as 3. Then, the $J(x)$ and its derivatives relevant to Eq.(2) can be evaluated as:

$$J(x)=3x^2,\quad J'(x)=6x,\quad J''(x)=6 \tag{6}$$

Then, Eq.(2) can be rewritten as:

$$\begin{aligned}-\frac{1}{4\mu}\left[\frac{1}{9x^4}\frac{\mathrm{d}^2}{\mathrm{d}x^2}+\frac{\mathrm{d}^2}{\mathrm{d}x^2}\frac{1}{9x^4}-\frac{4}{3x^6}\right]\cdot\\ \phi(x)+V(x)\phi(x)=E\phi(x)\end{aligned} \tag{7}$$

B. Finite element discrete variable representation

Generally speaking, the FE-DVR method [30] uses a combination of the finite element method and Gauss-Lobatto quadrature rule [59] to sample the working grid and establish the discrete variable representation. It is able to offer accurate numerical results for singular potential problems [45]. For details about this method, one can refer to Refs.[60−62]. The sampling procedure is performed in the following two steps. First, the working interval [x_{begin}, x_{end}] is divided into N_{e} equal elements [x^i, x^{i+1}]

$$x^i=i\times(x_{\mathrm{end}}-x_{\mathrm{begin}})+x_{\mathrm{begin}},\quad i=0,\ N_{\mathrm{e}} \tag{8}$$

Then within each element, N_{g} grid points x_m^i and weights w_m^i are generated according to the Gauss-Lobatto rule:

$$x_m^i=\frac{1}{2}[(x^{i+1}-x^i)x_m+(x^{i+1}+x_i)] \tag{9}$$

$$w_m^i=\frac{w_m}{2}(x^{i+1}-x_i) \tag{10}$$

where the the points x_m are defined as roots of the first derivative of Legendre polynomials $P_{N_{\mathrm{g}}-1}(x)$ according

DOI:10.1063/1674-0068/26/06/755-764

to

$$\frac{\mathrm{d}}{\mathrm{d}r}P_{N_\mathrm{g}-1}(x)|_{x=x_m}=0 \tag{11}$$

and the weights w_m are:

$$w_m=\frac{2}{N_\mathrm{g}(N_\mathrm{g}-1)[P_{N_\mathrm{g}-1}(x_m)]^2} \tag{12}$$

The basis functions have the explicit form

$$\chi_m^i(x)=\begin{cases}\dfrac{f_{N_\mathrm{g}}^{i-1}(x)+f_1^i(x)}{\sqrt{w_{N_\mathrm{g}}^{i-1}+w_1^i}}, & m=1 \ \text{(bridge)}\\ \dfrac{f_m^i(x)}{\sqrt{w_m^i}}, & \text{else (element)}\end{cases} \tag{13}$$

where the "bridge" function is used to ensure the communication between two adjacent elements. In particular, it guarantees the continuity of the wave function. The so-called Lagrange-Lobatto interpolating functions in Eq.(13) are defined as

$$f_m^i(x)=\prod_{k\neq m}\frac{x-x_k^i}{x_m^i-x_k^i}, \qquad x^i\le x\le x^{i+1} \tag{14}$$

Now let us consider the Hamiltonian matrix corresponding to Eq.(2) in the Hilbert space spanned by these basis functions. As these basis functions are orthonormalized and behave like weighted Dirac delta functions with regard to the generalized Gauss-Lobatto quadrature rule [60, 61], all the local operators ($V(x)$, $J(x)$, $J'(x)$, $J''(x)$) are diagonal in this space, and the diagonal elements correspond to their values on the numerical grid points. The kinetic operator is not diagonal, here we follow the derivation of Ref.[30] and obtain the matrix element as:

$$T_{mn}^{ij}=\frac{-1}{2\mu}\begin{cases}\dfrac{\delta_{ij}t_{mn}^i}{\sqrt{w_m^iw_n^i}}\\ (2\le m\le N_\mathrm{g}-1, \quad 2\le n\le N_\mathrm{g}-1)\\ \dfrac{\delta_{ij-1}t_{mn}^i}{\sqrt{w_m^i(w_1^j+w_{N_\mathrm{g}}^{j-1})}}+\dfrac{\delta_{ij}t_{mn}^i}{\sqrt{w_m^i(w_1^j+w_{N_\mathrm{g}}^{j-1})}}\\ (2\le m\le N_\mathrm{g}-1, \quad n=1)\\ \dfrac{\delta_{i-1j}t_{mn}^{i-1}}{\sqrt{w_n^j(w_1^i+w_{N_\mathrm{g}}^{i-1})}}+\dfrac{\delta_{ij}t_{mn}^i}{\sqrt{w_n^j(w_1^i+w_{N_\mathrm{g}}^{i-1})}}\\ (m=1, \quad 2\le n\le N_\mathrm{g}-1)\\ \dfrac{\delta_{ij}(t_{11}^i+t_{N_\mathrm{g}N_\mathrm{g}}^{i-1})+\delta_{ij-1}t_{11}^i+\delta_{i-1j}t_{N_\mathrm{g}-1}^{i-1}}{\sqrt{(w_1^i+w_{N_\mathrm{g}}^{j-1})\sqrt{(w_1^j+w_{N_\mathrm{g}}^{j-1})}}}\\ (m=1, \quad n=1)\end{cases} \tag{15}$$

and t_{mn}^i is given by

$$t_{mn}^i=\sum_k\frac{\mathrm{d}f_m^i(x_k^i)}{\mathrm{d}x}\frac{\mathrm{d}f_n^i(x_k^i)}{\mathrm{d}x}w_k^i \tag{16}$$

here, the differentiation matrix $\mathrm{d}f_m^i(x_k^i)/\mathrm{d}x$ can be evaluated as follows [63].

For $m\neq k$

$$\frac{\mathrm{d}f_m^i(x_k^i)}{\mathrm{d}x}=\frac{L_{N_s-1}(s_k)}{L_{N_\mathrm{g}-1}(s_m)}\frac{1}{x_m^i-r_k^i} \tag{17}$$

$$s_k=\frac{2x_k^i-(x^{i-1}+x_i)}{x^i-x^{i-1}} \tag{18}$$

where $L_{N_\mathrm{g}-1}(s)$ is the $N_\mathrm{g}-1$ order Legendre polynomial, for $m{=}k{=}2, 3, \ldots, N_\mathrm{g}-1$,

$$\frac{\mathrm{d}f_m^i(x_k^i)}{\mathrm{d}x}=0 \tag{19}$$

the first and last diagonal values can be found to be

$$\begin{aligned}\frac{\mathrm{d}f_1^i(x_1^i)}{\mathrm{d}x}&=\frac{\mathrm{d}f_{N_\mathrm{g}}^i(x_{N_\mathrm{g}}^i)}{\mathrm{d}x}\\ &=\frac{1}{2}\frac{N_\mathrm{g}(N_\mathrm{g}-1)}{x^i-x^{i-1}}\end{aligned} \tag{20}$$

Plus Eq.(15) and Eq.(6) into Eq.(2), then we can get the Hamiltonian matrix.

III. THE ONE-DIMENSIONAL COULOMB EXAMPLE

The singularity of Coulomb potential is notorious for a numerical calculation using spectral method. Many numerical methods have been proposed to deal with it. The FE-DVR method [30], the Coulomb function DVR method [64], the rational Chebyshev method [65], and Gauss-Legendre DVR [66] are among the best ones. In the following, the mapped finite element discrete variable representation will be applied in the eigenvalue and eigenfunction calculations for Coulomb potential, and the numerical results will show that the numerical efficiency of FE-DVR can be improved dramatically by the mapping procedure.

The energy levels of the hydrogen atom are the eigenvalues of

$$\left[-\frac{1}{2\mu}\frac{\mathrm{d}^2}{\mathrm{d}r^2}+\frac{l(l+1)}{2r^2}-\frac{1}{r}\right]\psi(r)=E\psi(r) \tag{21}$$

Eq.(21) has the analytical eigenfunctions

$$\psi(r)_{n,l}=r\exp\left(-\frac{r}{n}\right)\left(\frac{2r}{n}\right)^l L_{n+l}^{2l+1}\frac{2r}{n} \qquad (l=0,1,\ldots; \quad n\ge l+1) \tag{22}$$

with eigenvalues

$$E_n=-\frac{1}{2n^2} \tag{23}$$

where $L_n^m(x)$ is the generalized Laguerre polynomial [67]. n and l represent the principal and angular momentum quantum number respectively.

DOI:10.1063/1674-0068/26/06/755-764

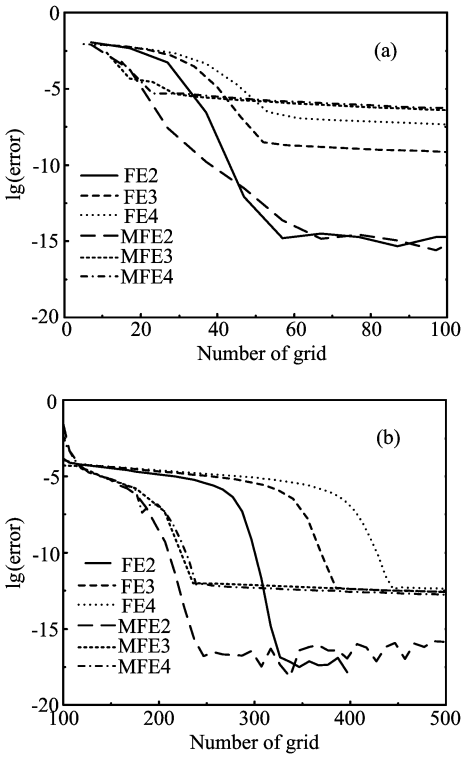

FIG. 1 Numerical convergence as a function of total grid number for the eigenvalue calculation of hydrogen atom. (a) and (b) present the results of the low (6th) and high (89th) lying states, respectively. The symbols FEn represents a FE-DVR with n elements, and MFEn represents a M-FE-DVR with n elements.

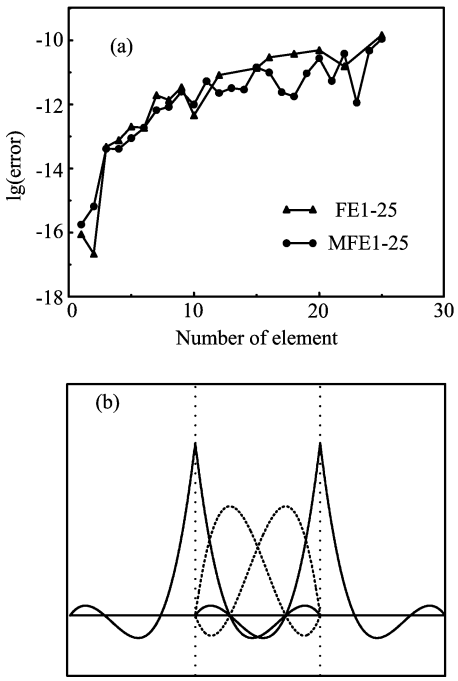

FIG. 2 (a) Eigenvalue convergence of the 89th bond state as a function of elements number (N_e) used in the calculations. (b) A sketch of some of the basis functions. The non-differential behavior of the "bridge" function (solid line) is clearly observed. The dotted line indicates the element.

A. Eigenvalue convergence

Numerical convergence using the FE-DVR and the M-FE-DVR for both high and low lying bound states of hydrogen atom is presented in Fig.1. Figure 1(a) gives the numerical convergence of the 6th eigenvalue with respect to the total number of grid points. In calculations for the results in Fig.1(a), the radial internal extends from 0 to 200 a.u. Similarly, Fig.1(b) gives the numerical convergence of the 89th eigenvalue. The corresponding radical internal extends from 0 to 2×10^4 a.u, since the eigenfunction of the 89th state ranges from 0 to 1.9×10^4 a.u.

The symbols FEn and MFEn in Fig.1 represent the numerical results calculated by the FE-DVR or the M-FE-DVR using n elements respectively. The numerical results in Fig.1(a) indicate that both the FE-DVR and M-FE-DVR have the comparable convergent speed. The reason is that for the low lying state, no more than 100 grid points distributing within a short radical internal can offer accuracy numerical results, so there is not so much space left for mapping procedure to improve the efficiency.

However, the results in Fig.1(b) indicate that the MFE2 scheme offers an accuracy of 10^{-17} with 250 grid points compared to the FE2 scheme which needs 320 grid points to get the same accuracy. We can find the same phenomenon from the comparison between MFE3, MFE4, and FE3, FE4 that the M-FE-DVR method has a faster convergence speed than the FE-DVR method. So the numerical results in Fig.1 indicate that the mapping procedure can improve the FE-DVR efficiency of obtaining high lying states in a large grid range.

Figure 1 also implies that the numerical accuracy of the FE-DVR or M-FE-DVR has limited value when the number of elements (N_e) increases. To illustrate this trend more intuitively, a collection of calculations with the number of elements varying from 1 to 25 and the total grid number fixed around 1200 was carried out. As is depicted in Fig.2(a), for both the FE-DVR and M-FE-DVR methods, the numerical accuracy decreases with the increasing of N_e. This phenomenon should be owing to the "bridge" function which is continuous and non-differentiable at the elements boundaries as shown in Fig.2(b). Therefore, even more elements can save computational effort, a usage of too many elements in the calculation for high accuracy calculations is not recommended.

In most grid-based numerical methods, we have domain truncation error since we cannot account for infinite grid region. Similar, the M-FE-DVR algorithm is accurate only for the eigenfunctions whose vibration is negligible at the edge of the physical interval region $[r_{\rm begin}, r_{\rm end}]$, but for the eigenfunctions extending

DOI:10.1063/1674-0068/26/06/755-764

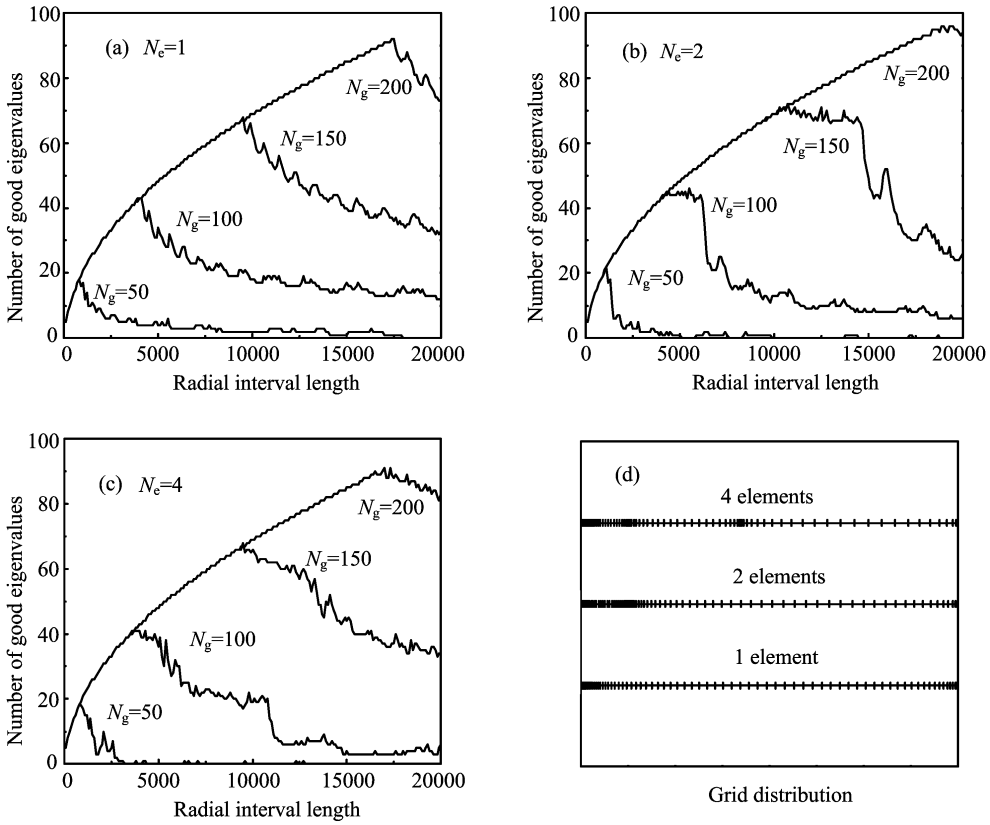

FIG. 3 (a), (b), and (c) present the number of accurate eigenvalues as a function of the radial interval length, calculated by the M-FE-DVR method with 1, 2, and 4 elements respectively. In each figure, the four lines represent different number of total grid (N_g) adopted in the calculations. (d) The grid distributions of the 1, 2, and 4 elements methods.

beyond the interval region $[r_{\rm begin}, r_{\rm end}]$, this method losses its accuracy rapidly. Therefore the errors of the M-FE-DVR algorithm consist of two parts. One part results from the domain truncation, and the other one results from numerical convergence, or basis truncation error. In the following discussion, we will illustrate in details how the two parts influence the total error.

Anyway, we note here that, in a calculation with grid range good enough, even the truncation "error" for a particular state is large, we still get accurate results. This can be understood in a spirit similar to that we can numerically simulate transmission of a plane wave in a finite grid range where we impose suitable boundary conditions.

Figure 3 depicts the number of accurate eigenvalues with respect to the length of the physical interval L adopted in the calculations. A M-FE-DVR with 1, 2, and 4 elements are shown in Fig.3 (a), (b) and (c) respectively. In each panel, there are four lines corresponding to different number of grid (N_g) adopted in the calculations. Here "accurate" means the relative error $|(E_{\rm exact}-E_{\rm numerical})/E_{\rm exact}|$ smaller than 10^{-3}. Figure 3(d) depicts the grid distribution of the 1, 2, and 4 elements M-FE-DVR methods. There is a peak on each curve depicted in Fig.3 (a)−(c). Due to the competition between the domain truncation error and the basis truncation error. And the two errors vary oppositely with L. When the total grid number is fixed, the larger L is, the smaller the domain truncation error will be, oppositely, the larger the basis truncation error will be. Therefore before the peak, the truncation is negligible and the domain truncation error contributes the major part to the total error. Conversely, after the peak, the domain truncation is negligible and the total error mainly comes from the basis truncation error.

In Fig.3(a), the curve decreases rather rapidly in the vicinity of the peak, which implies that the truncation error increase extremely fast with L. However, in Fig.3 (b) and (c) the decline trend in the vicinity of the peak is alleviated. The grid distribution of the 1, 2, and 4 elements situations are depicted in Fig.3(d). Figure 3(d) shows that about half of the grid points distributes within the r<2500 region in the 1 element situation, this is not quite reasonable for the higher eigenmodes whose eigenfunctions extend far beyond the r<2500 region, the grid points within the 5000−15000 region are too sparse to describe the rapid vibration of the eigenfunctions. In contrast, the 2 and 4 elements schemes perform better than the 1 element scheme in the aspect of grid distribution, more grid points are sampled in the center region. This more reasonable grid distribution can partly reduce the truncation error which makes

DOI:10.1063/1674-0068/26/06/755-764

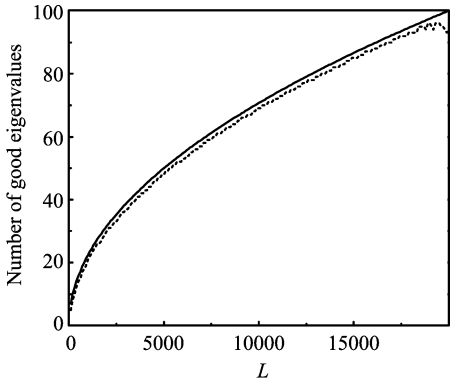

FIG. 4 The solid line indicates the number of good eigenvalues as a function of L calculated by a 2 elements M-FE-DVR with 200 grid points, and the dotted line corresponds to a function of L: $F(L)=\sqrt{L/2}$.

the curves in Fig.3 (b) and (c) decrease not so fast as those of Fig.3(a) after the peak.

Another interesting phenomenon can be found in Fig.3 (a)−(c): before the peak, all the curves coincide with each other. This indicates that the domain truncation error depends only on the physical interval length L and has no connection with the number of the grid points. The same conclusion can be derived from Fig.4 more intuitively. In Fig.4 the solid line depicts the number of good eigenvalues as a function of L calculated by a 2 elements M-FE-DVR with 200 grid points, and the dotted line corresponds to a function of L: $F(L)=\sqrt{L/2}$. Figure 4 reveals that the function of the number of good eigenvalues with respect to L follows close to $F(L)=\sqrt{L/2}$. This behavior can be understood by checking the eigenfunctions of the hydrogen atom [68]. As the average radial extents $\langle r\rangle$ of the eigenfunctions scale as the square of the principal quantum number, consequently the principal quantum number of the highest eigenmode within the region [0, L], which can be described by the M-FE-DVR method precisely, is around $\sqrt{L/2}$. Therefore the domain truncation error is determined by the radial interval length, and has nothing to do with the grid distribution or the grids amount.

B. Eigenfunction convergence

Next we study the convergence of eigenfunctions calculated by the M-FE-DVR method. In the calculations, the wave functions are represented on a set of discrete grid points. Therefore, values of the wave functions at positions other than the grid points have to be calculated by interpolation. The wave function can be interpolated as

$$\psi(r)=\sum_{i=0}^{N_{\rm e}-1}\sum_{j=1}^{N_{\rm g}-1}\psi(x_j^i)\chi_j^i[x(r)] \qquad (24)$$

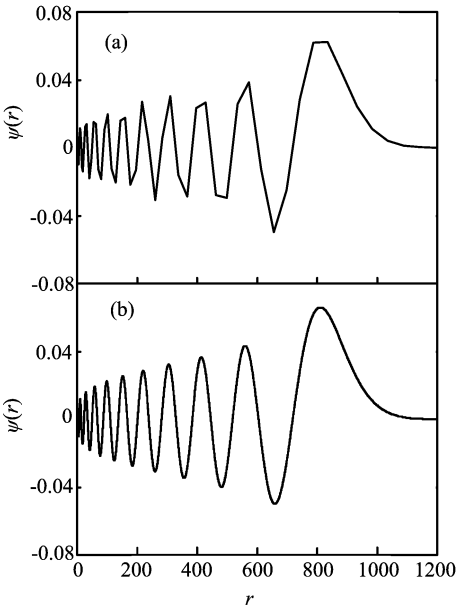

FIG. 5 The 21th normalized eigenfunction on the work grid points (a) and interpolated by Eq.(25) (b). The smoothness of the interpolated wavefunction may indicate that the wavefunction has been represented accurately, even the working grid points are quite sparse.

here, $\psi(x_j^i)$ is the value of eigenfunction on the working grid point x_j^i. Figure 5 (a) and (b) display the 21th normalized eigenfunction on the working grid points and interpolated by Eq.(24) respectively. A comparision between Fig.5 (a) and (b) may indicate the good quality of the polynomial interpolation of Eq.(24), even the original working grid points are sparse.

Figure 6 (a) and (b) presents the 21th and 34th eigenfunctions, respectively. In each figure, the numerical eigenfunction calculated by Eq.(24) and the corresponding exact one calculated by Eq.(22) are drawn. The numerical eigenfunctions are obtained by the 1 element scheme with 150 grid points distributed within an interval of 2500 a.u. Figure 5(a) shows that the eigenfunction of the 21 eigenmode is exactly consistent with the analytical one. However, the 34th numerical eigenfunction, shown in Fig.3(b), exhibits interesting feature. Even due to the domain truncation error, the wavefunction in the region around the right end of the grid is not consistent with the analytical one, the wavefunction in the inside region agrees with the analytical one well. This may suggest that the domain truncation error may be sensible to a particular eigenstate, but it may not influence the final dynamics results if we have imposed suitable boundary conditions.

C. Spurious states

As explained in Ref.[69], the mapping procedure invariably generate many eigenvalues and eigenfunctions which are poor approximations to the Schrödinger equa-

DOI:10.1063/1674-0068/26/06/755-764

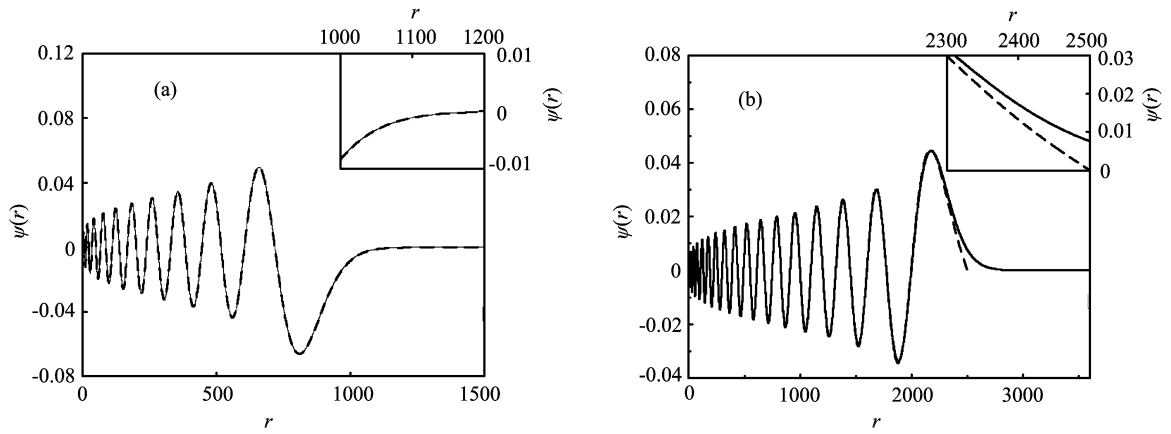

FIG. 6 Numerical (dashed) and exact analytical (solid) eigenfunctions of (a) 21th and (b) 34th eigenmodes.

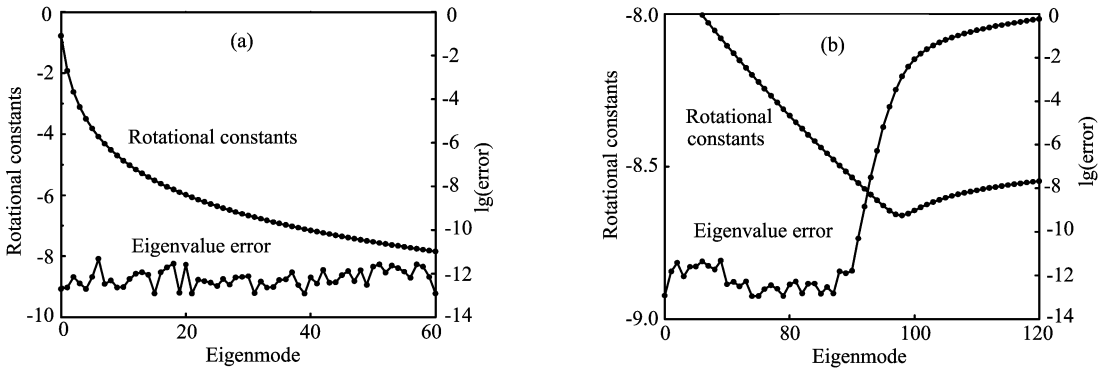

FIG. 7 Rotational constants and error of eigenvalues for vibrational levels of Coulomb potential.

tion. These inaccurate or "spurious" states was attributed to numerical errors in the derivatives $J'(x)$ and $J''(x)$ of the Jacobian, consequently detrimental to the accuracy description of the kinetic operator. These irregularities can be easily identified by their anomalous rotational constants B_v=1/(2$\mu\langle r^2\rangle$) [69]. To predict the "spurious" states, we present the rotational constants and eigenvalues accuracy of numerical eigenstates in Fig.7. These eigenstates corresponding to Fig.7 are calculated by the 1 element scheme with 300 grid points sampling from 0 to 2×10^4 a.u. In Fig.7, no irregularity appears in rotational constants of the first 95 eigenmodes. The first "spurious" appears at the 96th eigenmode with an accuracy of 10^{-3} for its eigenvalue. All the irregularities are associated with high lying states which should be owing to the domain truncation error. Therefore, if the radical interval is large enough, one do not need to worry about the "spurious" states in the M-FE-DVR scheme.

IV. VIBRATIONAL LEVEL CALCULATION FOR LONG-RANGE ALKALI DIMERS

In an ultra-cold condition and photoassociation experiment, one encounter with the long range potential

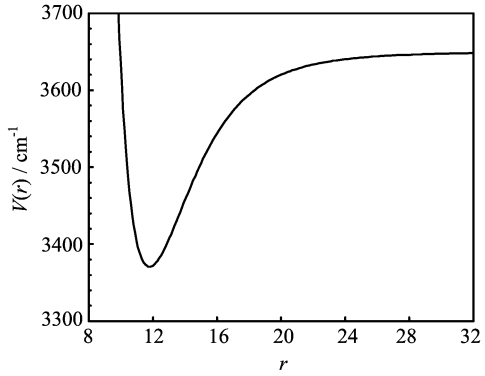

FIG. 8 The Cs_2 triplet ground state ($a^3\Sigma_u^+$) potential energy well.

of a molecule quite often. The mapped Fourier method has been applied for solving the photoassociation spectrum of $Rb_2(0_u^+)$ and $Cs_2(0_u^+)$ molecule with long-range potential [24, 64, 70, 71]. Here we take the potential energy curve of Cs_2 triplet ground state ($a^3\Sigma_u^+$ state) for the numerical illustration [72], which is plotted in Fig.8.

In Fig.9, we present the eigenvalue convergence with respect to total grid points for both the 5th and 50th

DOI:10.1063/1674-0068/26/06/755-764

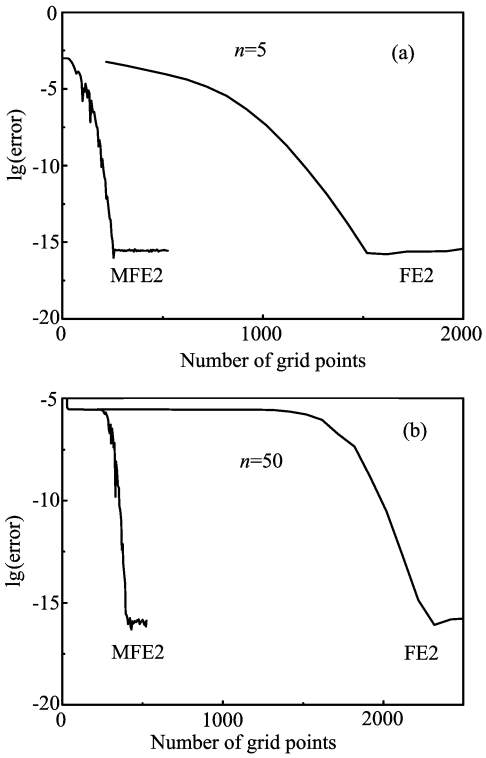

FIG. 9 Eigenvalue convergence as a function of total number of grid points used in the vibrational levels calculations of the Cs_2 triplet ground state. The numerical results are calculated by both the FE-DVR and M-FE-DVR methods with 2 elements. (a) and (b) correspond to the results of the 5th and 50th bound states, respectively. The M-FE-DVR method improves the numerical efficiency significantly.

bound states. These numerical results are calculated by the FE-DVR and M-FE-DVR with the radial interval extends from 7.5 a.u. to 1000 a.u. Here, we take the eigenvalues calculated by the widely used Sine-DVR [73] with 20000 grid points as the accurate values. In Fig.9, on can see that the M-FE-DVR method is capable of giving accurate eigenvalues for both high and low lying states with no more than 500 grid points. In contrast, the FE-DVR method needs more than 2000 grid points to get the same accuracy for high lying states.

In the calculations, totally 56 bound levels are found, and the wave function of the highest lying bond state is depicted in Fig.10. Figure 11 depicts the rotational constants for all the bound states. No irregularity is found in Fig.11 which indicates that there is no "spurious" state appearing in the 56 bound states calculated by the M-FE-DVR method. Figure 12 shows the eigenvalue accuracy for the first 200 eigenstates calculated by a 2 elements M-FE-DVR with 800 grid points. One can see that the eigenvalues can reach an accuracy better than 10^{-15} for the first 200 eigenstates. Therefore, the M-FE-DVR can improve the efficiency of grid distribution significantly and is a reliable and efficient tool for the description of long-range photoassociation

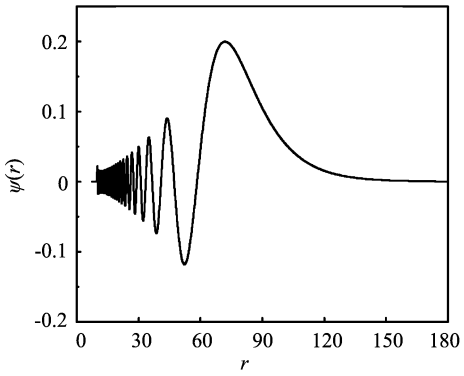

FIG. 10 The eigenfunction of the highest lying (56th) bound state for the Cs_2 triplet ground state.

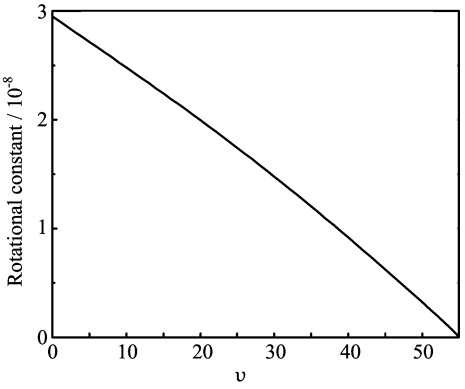

FIG. 11 Rotational constants of the first 56 vibrational levels for the Cs_2 triplet ground state.

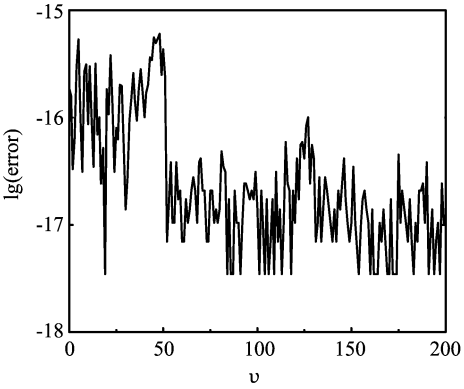

FIG. 12 Eigenvalue convergence of the first 200 vibrational levels for the Cs_2 triplet ground state.

problems.

V. CONCLUSION

In this work, a mapped FE-DVR method was developed for improving the grid points distribution of the original FE-DVR method. The proposed mapped FE-DVR has faster numerical convergence. At the same

DOI:10.1063/1674-0068/26/06/755-764

time, it is simple and can be implemented straightforward with the existing FE-DVR code. For the numerical illustration, the mapped FEDVR method is applied in eigenvalue and eigenfunction calculations for the one dimensional Coulomb potential of hydrogen atom and Cs_2 triplet ground state ($a^3\Sigma_u^+$) which has long range interaction potential. The numerical results indicate that the mapping procedure improves the grid distribution efficiency significantly, especially for the problems involving long-range alkali dimers. At the same time, the mapped procedure for the FE-DVR method surprisingly does not introduce any "ghost" state, which is often encountered in a mapped Fourier grid method.

VI. ACKNOWLEDGMENTS

This work was supported by the National Natural Science Foundation of China (No.21222308, No.21103187, and No.21133006), the Chinese Academy of Sciences, and the National Basic Research Program of China (No.2013CB922200).

[1] U. Manthe, H. D. Meyer, and L. S. Cederbaum, J. Chem. Phys. **97**, 3199 (1992).
[2] U. Manthe, H. D. Meyer, and L. S. Cederbaum, J. Chem. Phys. **97**, 9062 (1992).
[3] G. A. Worth, H. D. Meyer, and L. S. Cederbaum, J. Chem. Phys. **109**, 3518 (1998).
[4] G. A. Worth, H. D. Meyer, and L. S. Cederbaum, J. Chem. Phys. **105**, 4412 (1996).
[5] A. Raab, G. A. Worth, H. D. Meyer, and L. S. Cederbaum, J. Chem. Phys. **110**, 936 (1999).
[6] L. C. G. A. Worth and H. D. Meyer, Chem. Phys. Lett. **299**, 451 (1999).
[7] S. Mahapatra, G. A. Worth, H. D. Meyer, L. S. Cederbaum, and H. Köppel, J. Phys. Chem. A **105**, 5567 (2001).
[8] J. Y. Fang and H. Guo, J. Chem. Phys. **102**, 1944 (1995).
[9] T. Gerdts and U. Manthe, J. Chem. Phys. **107**, 6584 (1997).
[10] J. A. Baker, D. F. Kelley, and A. M. Kelley, J. Chem. Phys. **139**, 024702 (2013).
[11] F. Matzkies and U. Manthe, J. Chem. Phys. **108**, 4828 (1998).
[12] U. Manthe and F. Matzkies, J. Chem. Phys. **113**, 5725 (2000).
[13] E. M. Goldfield and S. K. Gray, J. Chem. Phys. **117**, 1604 (2002).
[14] A. Capellini and A. P. J. Jansen, J. Chem. Phys. **104**, 3366 (1996).
[15] M. Ehara, H. D. Meyer, and L. S. Cederbaum, J. Chem. Phys. **105**, 8865 (1996).
[16] R. Milot and A. P. J. Jansen, J. Chem. Phys. **109**, 1966 (1998).
[17] B. Jiang, J. Li, D. Xie, and H. Guo, J. Chem. Phys. **138**, 044704 (2013).
[18] D. Gottlieb and S. A. Orszag, *Numerical Analysis of Spectral Methods: Theory and Applications*, USA: Society for Industrial and Applied Mathematics, (1977).
[19] B. Fornberg, *A Practical Guide to Pseudospectral Methods*, Cambridge: Cambridge University Press, (1998).
[20] J. C. Light and T. Carrington, Adv. Chem. Phys. **114**, 263 (2007).
[21] Z. Bacic and J. C. Light, Annu. Rev. Phys. Chem. **40**, 469 (1989).
[22] E. Fattal, R. Baer, and R. Kosloff, Phys. Rev. E **53**, 1217 (1996).
[23] J. Echave and D. C. Clary, Chem. Phys. Lett. **190**, 225 (1992).
[24] V. Kokoouline, O. Dulieu, R. Kosloff, and F. Masnou-Seeuws, J. Chem. Phys. **110**, 9865 (1999).
[25] M. Nest and P. Saalfrank, J. Chem. Phys. **113**, 8753 (2000).
[26] I. Degani, J. Chem. Phys. **128**, (2008).
[27] S. Cohen and S. I. Themelis, J. Chem. Phys. **124**, (2006).
[28] A. G. Borisov, J. Chem. Phys. **114**, 7770 (2001).
[29] H. D. M. M. Nest, Chem. Phys. Lett. **352**, 486 (2002).
[30] T. N. Rescigno and C. W. McCurdy, Phys. Rev. A **62**, 032706 (2000).
[31] R. W. D.E. Manolopoulos, Chem. Phys. Lett. **152**, 23 (1988).
[32] L. A. C. Barry and I. Schneider, J. Non-Cryst. Solids **351**, 1551 (2005).
[33] S. X. Hu, Phys. Rev. E **81**, 056705 (2010).
[34] S. X. Hu and L. A. Collins, Phys. Rev. Lett. **96**, 073004 (2006).
[35] B. Schneider, J. Feist, S. Nagele, R. Pazourek, S. Hu, L. A. Collins, and J. Burgdörfer, *Quantum Dynamic Imaging, CRM Series in Mathematical Physics*, New York: Springer, 149 (2011).
[36] H. Suno, J. Chem. Phys. **134**, 064318 (2011).
[37] L. Tao, C. W. McCurdy, and T. N. Rescigno, Phys. Rev. A **79**, 012719 (2009).
[38] S. X. Hu, L. A. Collins, and B. I. Schneider, Phys. Rev. A **80**, 023426 (2009).
[39] L. Tao, C. W. McCurdy, and T. N. Rescigno, Phys. Rev. A **80**, 013402 (2009).
[40] F. L. Yip, C. W. McCurdy, and T. N. Rescigno, Phys. Rev. A **81**, 053407 (2010).
[41] K. Balzer, S. Bauch, and M. Bonitz, Phys. Rev. A **82**, 033427 (2010).
[42] D. J. Haxton, K. V. Lawler, and C. W. McCurdy, Phys. Rev. A **83**, 063416 (2011).
[43] K. Balzer, S. Bauch, and M. Bonitz, Phys. Rev. A **81**, 022510 (2010).
[44] B. I. Schneider, L. A. Collins, and S. X. Hu, Phys. Rev. E **73**, 036708 (2006).
[45] B. I. Schneider and N. Nygaard, Phys. Rev. E **70**, 056706 (2004).
[46] P. S. Julienne and J. Vigué, Phys. Rev. A **44**, 4464 (1991).
[47] H. R. Thorsheim, J. Weiner, and P. S. Julienne, Phys. Rev. Lett. **58**, 2420 (1987).
[48] P. D. Lett, K. Helmerson, W. D. Phillips, L. P. Ratliff, S. L. Rolston, and M. E. Wagshul, Phys. Rev. Lett. **71**, 2200 (1993).
[49] J. D. Miller, R. A. Cline, and D. J. Heinzen, Phys. Rev. Lett. **71**, 2204 (1993).

DOI:10.1063/1674-0068/26/06/755-764

[50] J. Ulmanis, J. Deiglmayr, M. Repp, R. Wester, and M. Weidemller, Chem. Rev. **112**, 4890 (2012).
[51] D. E. L. R. D. Glover, J. E. Calvert, and R. T. Sang, J. Phys. B **44**, 2425202 (2011).
[52] J. E. C. R. D. Glover and R. T. Sang, Phys. Rev. A **87**, 023415 (2013).
[53] E. Luc-Koenig, R. Kosloff, F. Masnou-Seeuws, and M. Vatasescu, Phys. Rev. A **70**, 033414 (2004).
[54] C. P. Koch, F. m. c. Masnou-Seeuws, and R. Kosloff, Phys. Rev. Lett. **94**, 193001 (2005).
[55] A. Merli, F. Eimer, F. Weise, A. Lindinger, W. Salzmann, T. Mullins, S. Götz, R. Wester, M. Weidemüller, R. Ağanoğlu, and C. P. Koch, Phys. Rev. A **80**, 063417 (2009).
[56] C. P. Koch, M. Ndong, and R. Kosloff, Faraday Discuss. **142**, 389 (2009).
[57] W. Skomorowski, F. Pawlowski, C. P. Koch, and R. Moszynski, J. Chem. Phys. **136**, 194306 (2012).
[58] D. Lemoine, Chem. Phys. Lett. **320**, 492 (2000).
[59] V. Krylov, *Approximate Calculation of Integrals*, New York: Dover Publication, (1962).
[60] R. W. D. E. Manolopoulos, Chem. Phys. Lett. **152**, 23 (1988).
[61] K. Balzer, S. Bauch, and M. Bonitz, Phys. Rev. A **81**, 022510 (2010).
[62] K. Balzer, S. Bauch, and M. Bonitz, J. Phys.: Conf. Ser. **220**, 012020 (2010).
[63] C. Pozrikidis, *Introduction to Finite and Spectral Element Methods using MATLAB*, Chapman & Hall/CRC, 165 (2005).
[64] J. Q. W. Lo and B. D. Shizgal, J. Phys. B **41**, 185103 (2008).
[65] P. B. John P. Boyd, and C. Rangan, J. Comput. Phys. **188**, 56 (2003).
[66] B. I. Schneider, Phys. Rev. A **55**, 3417 (1997).
[67] M. Abramowitz and I. A. Stegun, *Handbook of Mathematical Functions*, Natl. Bur. Std. US, (1964).
[68] H. S. Friedrich, *Theoretical Atomic Physics*, New York: Springer, (1990).
[69] K. Willner, O. Dulieu, and F. Masnou-Seeuws, J. Chem. Phys. **120**, 548 (2004).
[70] E. Fattal, R. Baer, and R. Kosloff, Phys. Rev. E **53**, 1217 (1996).
[71] V. Kokoouline, O. Dulieu, and F. Masnou-Seeuws, Phys. Rev. A **62**, 022504 (2000).
[72] F. Xie, V. B. Sovkov, A. M. Lyyra, D. Li, S. Ingram, J. Bai, V. S. Ivanov, S. Magnier, and L. Li, J. Chem. Phys. **130**, (2009).
[73] J. C. Light, I. P. Hamilton, and J. V. Lill, J. Chem. Phys. **82**, 1400 (1985).

DOI:10.1063/1674-0068/26/06/755-764